

## SUPERCONDUCTIVITY

## Clean 2D superconductivity in a bulk van der Waals superlattice

A. Devarakonda<sup>1</sup>, H. Inoue<sup>1\*</sup>, S. Fang<sup>2†</sup>, C. Ozsoy-Keskinbora<sup>3‡</sup>, T. Suzuki<sup>1</sup>, M. Kriener<sup>4</sup>, L. Fu<sup>1</sup>, E. Kaxiras<sup>2,3</sup>, D. C. Bell<sup>3,5</sup>, J. G. Checkelsky<sup>1§</sup>

Advances in low-dimensional superconductivity are often realized through improvements in material quality. Apart from a small group of organic materials, there is a near absence of clean-limit two-dimensional (2D) superconductors, which presents an impediment to the pursuit of numerous long-standing predictions for exotic superconductivity with fragile pairing symmetries. We developed a bulk superlattice consisting of the transition metal dichalcogenide (TMD) superconductor 2H-niobium disulfide (2H-NbS<sub>2</sub>) and a commensurate block layer that yields enhanced two-dimensionality, high electronic quality, and clean-limit inorganic 2D superconductivity. The structure of this material may naturally be extended to generate a distinct family of 2D superconductors, topological insulators, and excitonic systems based on TMDs with improved material properties.

Superconducting states with real- or momentum-space nodes in the gap function are acutely sensitive to disorder. Such nodal pairing states are weakened by the momentum-space averaging of the gap function caused by disorder-induced scattering of Cooper pairs across the Fermi surface. Conventionally, this disorder averaging can be avoided when Cooper pairs have well-defined crystal momentum  $k$  within the Pippard coherence length  $\xi_0$ ; this regime is realized when  $\xi_0$  is smaller than the electronic mean free path  $\ell$  (i.e.,  $\xi_0/\ell \ll 1$ ). Two-dimensional superconductors in this so-called clean limit play a central role in proposals including archetypal platforms for finite-momentum Cooper pairing (1, 2) and recent constructions for unconventional superconducting phases that leverage normal-state spin textures (3, 4). At present, there is a paucity of materials that allow access to this regime.

Figure 1A presents a historical survey of superconducting materials sorted according to their dimensionality and cleanliness, the former characterized by  $H_{c2}^c/H_{c2}^a$  (the ratio of the upper critical magnetic fields perpendicular and parallel to the 2D layer) and the latter by  $\xi_0/\ell$ . Early experimental work in granular Al ( $g$ -Al) and amorphous Bi ( $\alpha$ -Bi) films demonstrated 2D superconductivity through precise control of the superconducting layer thickness; these systems were later used in

groundbreaking studies that observed the vortex-antivortex unbinding transition of Berezinskii-Kosterlitz-Thouless (BKT) that had been predicted for 2D superconductors (5). Shortly thereafter, studies of similar films revealed that the disorder induced a superconductor-insulator transition in two dimensions (6). Further developments in thin-film growth have led to the observation of the BKT transition in crystalline films of Nb ( $c$ -Nb) (7) and, more recently, to high-quality 2D superconductors formed at epitaxial interfaces in LaAlO<sub>3</sub>/SrTiO<sub>3</sub> (8) and in  $\delta$ -doped Nb-SrTiO<sub>3</sub> (9).

In parallel, the study of anisotropic bulk superconductors has also yielded substantial insight into the nature of the superconducting state. These materials can also be framed in the context of 2D superconductivity (see Fig. 1A); prototypical examples include cuprates, pnictides, organic charge-transfer salts, graphite intercalation compounds, and transition metal dichalcogenides (TMDs). Considerable effort has been invested in pursuing tunable dimensionality in these systems. For example, the search for new cuprates in the Ruddlesden-Popper series and their oxygen-deficient variants (10) has led to a diverse set of materials with variable dimensionality and a rich variety of exotic behavior (11). Discovery of the structurally related layered perovskite Sr<sub>2</sub>RuO<sub>4</sub> realized a 2D stoichiometric superconductor well within the clean limit, in principle satisfying the stability requirements for fragile superconducting gap functions that would otherwise be disrupted by nonmagnetic disorder (12). Despite a great deal of interest in such phases, this very clean and highly 2D regime has largely been limited to organic systems (13).

Substantial efforts have gone toward achieving 2D superconductivity in TMDs, which, given their intrinsically strong spin-orbit coupling and inversion symmetry breaking, are expected to yield exotic forms of superconductivity in the clean limit (14). As shown in

Fig. 1A for the case of 2H-TaS<sub>2</sub>, intercalation of organic molecules (15) [(Py)<sub>0.5</sub>-TaS<sub>2</sub>, where Py is pyridine] and incommensurate spacer layers (16) [(PbS)<sub>1.13</sub>TaS<sub>2</sub>] has been used to drive these materials toward the 2D limit and reduce the inversion-symmetric coupling between adjacent layers (17). These have led to important advances, such as establishing that superconductivity is a property of the 2D planes in (Py)<sub>0.5</sub>-TaS<sub>2</sub>. More recently, developments in the exfoliation of van der Waals (vdW) layered materials have made atomically thin 2D superconductors more readily accessible (e.g., ML-TaS<sub>2</sub>) (18–21). Subsequent studies have revealed a form of superconductivity characterized by strong Ising spin-orbit coupling equivalent to applying magnetic fields on the order of 100 T (19–21). However, flakes exfoliated from the bulk are often subject to degradation and reduction in quality during the fabrication process (22). Here, we show that high-quality H-NbS<sub>2</sub> monolayers with electronic mobilities more than three orders of magnitude larger than in bulk 2H-NbS<sub>2</sub> can be realized in a bulk single-crystal superlattice formed with a commensurate block layer. Correspondingly, we find that this material is a clean-limit 2D superconductor exhibiting a BKT transition at  $T_{\text{BKT}} = 0.82$  K and prominent 2D Shubnikov-de Haas (SdH) quantum oscillations.

The fundamental structural unit in hexagonal TMDs is the  $H\text{-}MX_2$  layer, where  $M$  and  $X$  are a transition metal and chalcogen, respectively. As shown in Fig. 1B, this structure [point group symmetry  $\bar{6}m2$  ( $D_{3h}$ )] breaks inversion symmetry in the layer plane owing to the trigonal prismatic coordination of  $X$  around  $M$  (the missing inversion partners are shown as dashed circles), and as a result yields an out-of-plane (Ising) spin texture (18–21). For thin flakes deposited on substrates, the substrate-flake interface breaks mirror symmetry (Fig. 1C) and yields an in-plane (Rashba) spin texture (23). Taken together, for TMD flakes on substrates, the simultaneous breaking of mirror and inversion symmetry leads to a mixed spin texture (Fig. 1D) on the Fermi surface composed of both Ising and Rashba components (18). These spin textures and the resulting physics are suppressed in the bulk limit, where the overall unit cell preserves inversion symmetry.

We have synthesized a single-crystal material, Ba<sub>9</sub>Nb<sub>11</sub>S<sub>28</sub>, composed of high-quality H-NbS<sub>2</sub> layers and Ba<sub>3</sub>NbS<sub>5</sub> block layers in which the TMD layers are strongly decoupled (17). Figure 1E shows a cross section of the structure imaged by high-angle annular dark-field scanning transmission electron microscopy (HAADF-STEM) with the model structure superimposed. As determined by electron and powder x-ray diffraction, the unit cell (space group  $P\bar{3}1c$  with  $a = 10.4$  Å,  $c = 24.5$  Å) is composed of two inversion-related H-NbS<sub>2</sub> layers across each of which mirror symmetry is broken by the

<sup>1</sup>Department of Physics, Massachusetts Institute of Technology, Cambridge, MA 02139, USA. <sup>2</sup>Department of Physics, Harvard University, Cambridge, MA 02138, USA. <sup>3</sup>John A. Paulson School of Engineering and Applied Sciences, Harvard University, Cambridge, MA 02138, USA. <sup>4</sup>RIKEN Center for Emergent Matter Science (CEMS), Wako 351-0198, Japan. <sup>5</sup>Center for Nanoscale Systems, Harvard University, Cambridge, MA 02138, USA.

\*Present address: Institute for Materials Research, Tohoku University, Sendai, Miyagi 980-8577, Japan.

†Present address: Department of Physics and Astronomy, Center for Materials Theory, Rutgers University, Piscataway, NJ 08854, USA.

‡Present address: Thermo Fisher Scientific, 5600KA Eindhoven, Netherlands.

§Corresponding author. Email: checkelsky@mit.edu

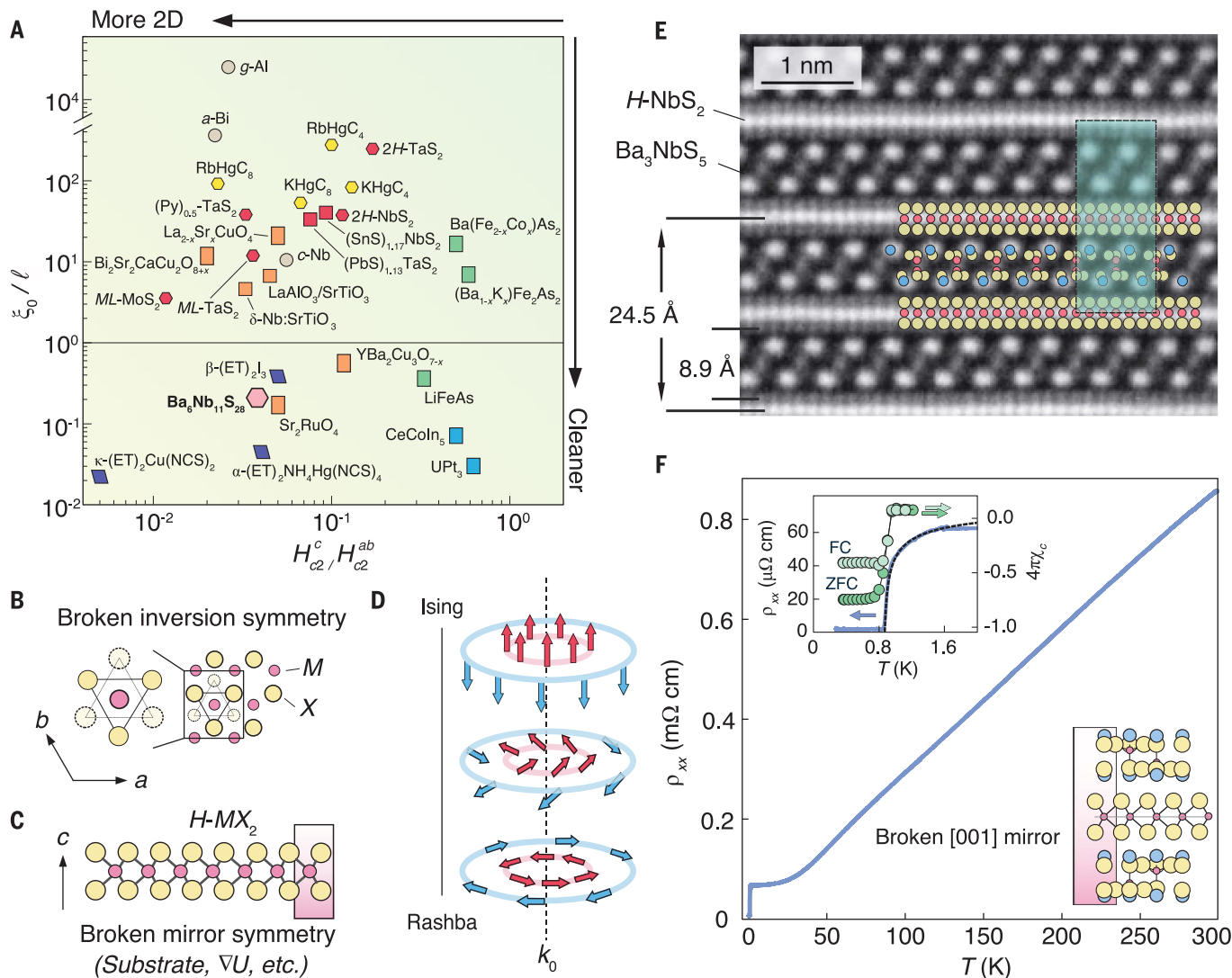


**Fig. 1. 2D superconductivity and  $\text{Ba}_6\text{Nb}_{11}\text{S}_{28}$ .** (A) Survey of superconducting materials characterized by anisotropy of the upper critical field  $H_{c2}^c/H_{c2}^{ab}$  and ratio of the Pippard coherence length to mean free path  $\xi_0/\ell$ . The boundary between the clean and dirty limits is shown as a horizontal line. (B) Crystal structure of  $H\text{-MX}_2$  projected onto the  $ab$ -plane. Lack of inversion symmetry is illustrated by the missing chalcogen (X) inversion partners (dashed circles). (C) The  $ab$ -plane mirror symmetry in monolayer  $H\text{-MX}_2$  can be broken by substrates or local fields ( $\nabla U$ ). (D) Depiction of momentum space spin-orbit texture for monolayer  $H\text{-MX}_2$  with varying degrees of

Ising and Rashba coupling. (E) HAADF-STEM image of  $\text{Ba}_6\text{Nb}_{11}\text{S}_{28}$  taken along the  $[1\bar{1}00]$  axis (scale bar, 1 nm). A simulation of the model structure is overlaid with one unit cell shaded in green. Ba, Nb, and S atoms are depicted as blue, red, and yellow circles, respectively. (F) Resistivity as a function of temperature  $\rho_{xx}(T)$  in  $\text{Ba}_6\text{Nb}_{11}\text{S}_{28}$  showing the superconducting transition. Upper inset: Magnified view of the transition in  $\rho_{xx}(T)$  and magnetic susceptibility  $4\pi\chi_c$  measured with zero field cooling (ZFC) and field cooling (FC).  $\rho_{xx}(T)$  is well fit by the Halperin-Nelson model shown in black (see text). Lower inset:  $H\text{-NbS}_2$  layer and mirror symmetry-breaking  $\text{Ba}_3\text{NbS}_5$  block layers.

neighboring block layers; the overall unit cell retains inversion symmetry. The  $H\text{-NbS}_2$  interlayer distance  $d = 8.9 \text{ \AA}$  is more than three times that of  $2H\text{-NbS}_2$  (24), leading to a reduction of the interlayer transfer integral  $t_{\perp}$ . This amplifies the two-dimensionality of the electronic structure relative to  $2H\text{-NbS}_2$  and enables local symmetry breaking-induced spin-orbit textures on the  $H\text{-NbS}_2$  layers (25, 26). [ $H\text{-NbS}_2$  monolayers in  $\text{Ba}_6\text{Nb}_{11}\text{S}_{28}$  experience local inversion symmetry breaking with point group symmetry  $32 (D_3)$  (17).] Whereas traditional misfit compounds combine incommensurate layers in a superlattice,

$\text{Ba}_6\text{Nb}_{11}\text{S}_{28}$  exhibits a  $3 \times 3$  in-plane, commensurate superstructure caused by the difference in in-plane lattice constants between the two layer types (17), which leads to additional modification of the electronic structure.

Figure 1F shows the dependence of electrical resistivity  $\rho_{xx}(T)$  on temperature  $T$  for  $\text{Ba}_6\text{Nb}_{11}\text{S}_{28}$ . The system is a metal, eventually showing superconductivity below  $T = 1 \text{ K}$ . This can be compared to bulk  $2H\text{-NbS}_2$ , which is also metallic and becomes a superconductor at critical temperature  $T_c = 5.7 \text{ K}$ . Unlike several other related  $H\text{-MX}_2$  systems, neither  $\text{Ba}_6\text{Nb}_{11}\text{S}_{28}$  nor  $2H\text{-NbS}_2$  shows signs of a den-

sity wave transition (17, 27). The upper inset of Fig. 1F shows a detailed view of the superconducting transition, which shows onset near  $T = 1.6 \text{ K}$  and reaches zero resistance at  $T = 0.85 \text{ K}$ . At the latter temperature, the magnetic susceptibility  $4\pi\chi_c$  with field along the  $c$  axis shows a Meissner signal reaching a shielding fraction of 75% (Fig. 1F, upper inset, dark green ZFC data points) and a volume fraction of 40% (Fig. 1F, upper inset, light green FC data points). The reduction in the transition temperature for the  $\text{NbS}_2$  layers relative to the bulk is similar to that observed in organic intercalated variants (28) and is consistent with

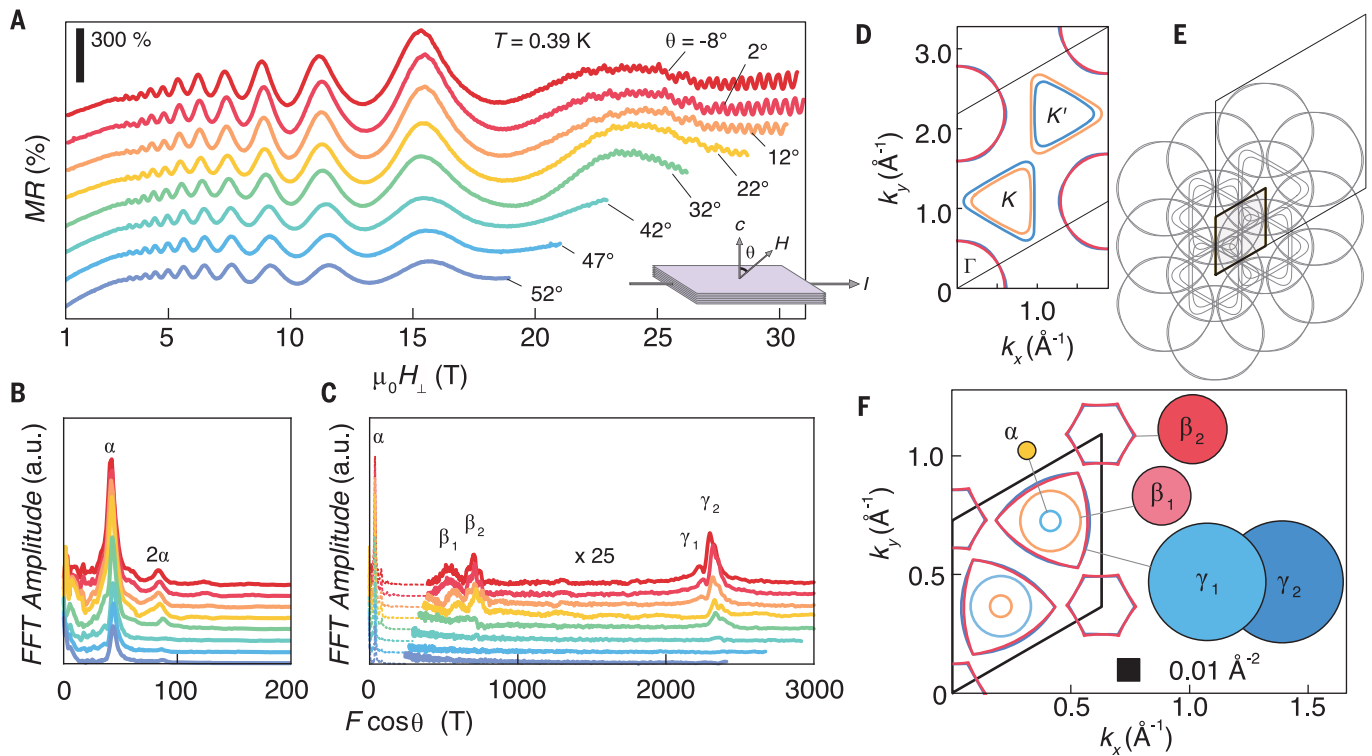


**Fig. 2. Quantum oscillations and electronic structure of  $\text{Ba}_6\text{Nb}_{11}\text{S}_{28}$ .** (A) Magnetoresistance as a function of perpendicular field  $MR \equiv [\rho_{xx}(\mu_0 H_\perp) / \rho_{xx}(0)] - 1$  at temperature  $T = 0.39$  K for different field rotation angles  $\theta$  (geometry defined as shown in the inset). Curves are vertically offset by 150% of  $MR$  for clarity. (B and C) Low-frequency range (B) and full range (C) of quantum oscillation amplitude FFT as a function of perpendicular frequency  $F \cos \theta$ . The FFT amplitudes for the higher-frequency pockets are multiplied

by 25. (D) DFT calculation of monolayer  $H\text{-NbS}_2$  Fermi surfaces including spin-orbit coupling (17). (E) Depiction of zone-folding scheme involving the  $3 \times 3$  superstructure imposed by the  $\text{Ba}_3\text{NbS}_5$  block layer where the reduced Brillouin zone is enclosed by the bold line. (F) Electronic structure of zone-folded monolayer  $H\text{-NbS}_2$  with experimentally observed Fermi surface cross-sectional areas drawn to scale as solid circles. The black box corresponds to  $0.01 \text{ \AA}^{-2}$ .

a reduction of the electron-phonon coupling strength inferred from the measured resistivity at high  $T$  (17).

The temperature dependence of resistivity for  $0.85 \text{ K} < T < 1.6 \text{ K}$  is well described by the Halperin-Nelson model,  $\rho_{xx}^F(T) = \rho_{xx}^N \exp(-b/\sqrt{t})$ , where  $\rho_{xx}^F$  and  $\rho_{xx}^N$  are the fluctuation and normal-state resistivity, respectively;  $t = (T/T_{\text{HN}}) - 1$ ; and  $b$  is a fitting parameter on the order of 1 (Fig. 1F, upper inset, dashed curve) (29). The agreement with the Halperin-Nelson model evidences fluctuations of the superconducting order parameter above a two-dimensional BKT transition. Such behavior is generally rare in bulk single crystals but has been reported in  $\text{La}_{1.875}\text{Ba}_{0.125}\text{CuO}_4$  and attributed to the decoupling of superconducting  $\text{CuO}_2$  planes by stripe order (30). This is a further departure from the behavior in bulk  $2H\text{-NbS}_2$ , which exhibits a sharp superconducting transition (17) (fig. S23); instead, it closely resembles those observed in monolayer  $H\text{-MX}_2$ . Further evidence of increased two-dimensionality is the resistivity anisotropy  $\rho_{zz}/\rho_{xx} > 10^3$  at low  $T$  in the normal state of  $\text{Ba}_6\text{Nb}_{11}\text{S}_{28}$  (where  $\rho_{zz}$  is the  $c$ -axis resistivity), which is substan-

tially enhanced relative to  $\rho_{zz}/\rho_{xx} \sim 100$  in  $2H\text{-NbS}_2$  (17) (fig. S24).

Magnetotransport measurements demonstrate the cleanliness of this material and show further evidence for a 2D electronic structure. Figure 2A shows the magnetoresistance  $MR \equiv [\rho_{xx}(H)/\rho_{xx}(0)] - 1$ , measured to 31 T. We observe SDH quantum oscillations that respond to the component of the magnetic field perpendicular to the  $ab$ -plane (the tilt angle  $\theta$  is measured between the  $c$  axis and the applied field). The fast Fourier transform (FFT) computed after subtracting a monotonically increasing background (17) (fig. S14) plotted versus inverse field shows this more clearly (Fig. 2, B and C). Here, the oscillation frequency multiplied by  $\cos(\theta)$  has little variance versus angle, demonstrating the 2D nature of the Fermi surface. This is qualitatively different from  $2H\text{-NbS}_2$ , for which electronic structure calculations indicate warped and elliptical Fermi surfaces (31). Owing to the reduced coupling between the TMD layers, the observed bands (labeled here as  $\alpha$ ,  $\beta_1$ ,  $\beta_2$ ,  $\gamma_1$ , and  $\gamma_2$ ) can be understood by starting with the 2D electronic structure of monolayer  $H\text{-NbS}_2$ , which consists of bands at the  $\Gamma$ ,  $K$ , and  $K'$

points of the hexagonal Brillouin zone (Fig. 2D), and zone folding into the reduced Brillouin zone determined by the  $3 \times 3$  superstructure imposed by the block layers (Fig. 2E). In particular, the reduction in the pocket size from monolayer  $H\text{-NbS}_2$  caused by zone folding, approximately one order of magnitude, quantitatively captures the size of the observed pockets (Fig. 2F) and is further supported by first-principles calculations (17) (fig. S12). An important aspect of this structure is that the large ratio of the spin-orbit coupling to  $t_\perp$ , evident from the degree of two-dimensionality, enables local symmetry breaking to affect the bulk electronic structure. The zone folding promotes the Rashba-textured pockets associated with the  $\Gamma$  point in monolayer  $H\text{-NbS}_2$  to be larger than the Ising-split pockets at  $K$  and  $K'$  [supported by comparing the calculated band structure for monolayer  $H\text{-NbS}_2$  with that of the  $3 \times 3$  zone-folded structure (17) (figs. S11 and S12)] and has potential implications for superconducting pairing.

More generally, it is noteworthy that quantum oscillations have not been reported in  $2H\text{-NbS}_2$ ; there, the typical transport mobilities reported for bulk single crystals are on the



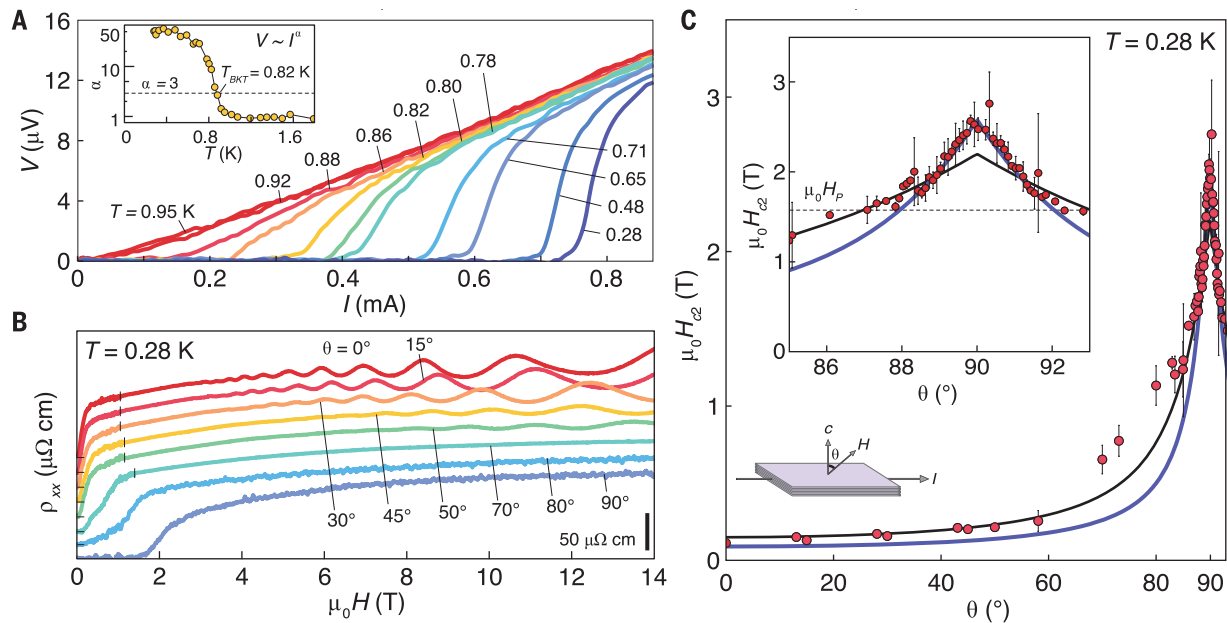


**Fig. 3. 2D superconductivity and Pauli limit breaking in  $\text{Ba}_6\text{Nb}_{11}\text{S}_{28}$ .**

(A) Current-voltage characteristics  $I(V)$  from  $T = 0.95$  K to  $T = 0.28$  K. The inset shows the evolution of the power law  $V \propto I^\alpha$ ; the horizontal line marks  $\alpha = 3$ . (B) Longitudinal resistivity  $\rho_{xx}$  as a function of field  $\mu_0 H$  for different values of  $\theta$ . Curves are vertically offset by  $20 \mu\Omega \text{ cm}$  for clarity (horizontal lines). Vertical ticks separate regions measured with low current ( $7 \mu\text{A}$ ) and higher current ( $70 \mu\text{A}$ ) to avoid suppression of

superconductivity by Joule heating. For  $\theta = 80^\circ$  and  $90^\circ$ , only low current is used.

(C) Angular dependence of upper critical field  $\mu_0 H_{c2}$  measured at  $T = 0.28$  K with fits to the 2D-Tinkham model, computed using data in the range  $|\theta - 90^\circ| < 1.7^\circ$  (purple curve) and  $|\theta - 90^\circ| > 1.7^\circ$  (black curve), respectively. The inset shows a detailed view near  $\theta = 90^\circ$  where an enhancement of  $\mu_0 H_{c2}(\theta)$  is observed across the Pauli limit  $\mu_0 H_P$ . We define  $\mu_0 H_{c2}$  and its error to be when  $\rho_{xx}$  reaches  $50 \pm 5\%$  of the normal-state value.

order of  $1 \text{ cm}^2 \text{ V}^{-1} \text{ s}^{-1}$  (27). In  $\text{Ba}_6\text{Nb}_{11}\text{S}_{28}$ , we see the onset of SdH quantum oscillations in magnetic fields between 2 and 3 T, indicating quantum mobilities on the order of  $10^3 \text{ cm}^2 \text{ V}^{-1} \text{ s}^{-1}$ . Analysis of the quantum oscillations and low-field magnetoresistance indicates an associated transport mean free path  $\ell = 1.21 \mu\text{m}$ , which greatly exceeds the Pippard coherence length  $\xi_0 \approx 0.18 \hbar v_F / k_B T_c = 254 \text{ nm}$  (where  $\hbar$  is the Planck constant divided by  $2\pi$ ,  $v_F$  is the Fermi velocity, and  $k_B$  is the Boltzmann constant) (17). This places  $\text{Ba}_6\text{Nb}_{11}\text{S}_{28}$  in the clean limit of superconductivity (Fig. 1A).

Turning to properties of the superconducting state, Fig. 3A shows the current-voltage  $I(V)$  characteristics of  $\text{Ba}_6\text{Nb}_{11}\text{S}_{28}$  across the superconducting transition. As expected for a BKT transition (29), a linear response at  $T = 0.95$  K and above crosses over to a nonlinear dependence  $V \propto I^\alpha$  with  $\alpha \sim 3$  at  $T_{\text{BKT}} = 0.82$  K, consistent with  $T_{\text{HN}} = 0.85$  K. With further examination of the fluctuation conductivity and the slope of the power-law exponent close to  $T_{\text{BKT}}$ , we find evidence for a vanishingly small interlayer coupling in the superconducting state (17, 32). Figure 3B shows the evolution of  $\rho_{xx}(H)$  as a function of magnetic field for different values of  $\theta$ . Whereas for  $\theta = 0^\circ$  superconductivity is suppressed with relatively low fields and gives rise to quantum oscillations, for larger  $\theta$  the upper critical field  $\mu_0 H_{c2}$  rapidly increases (we define  $\mu_0 H_{c2}$  and its error to be when  $\rho_{xx}$  reaches  $50 \pm 5\%$  of

the normal-state value). Figure 3C summarizes this behavior, with  $\mu_0 H_{c2}(\theta)$  showing a sharp cusp in in-plane fields. Recent studies of 2D superconductors have shown that a feature that distinguishes such systems from anisotropic 3D superconductors is the profile of  $\mu_0 H_{c2}(\theta)$  following the 2D Tinkham form

$$\left( \frac{H_{c2}(\theta) \sin \theta}{H_{c2}^{ab}} \right)^2 + \left| \frac{H_{c2}(\theta) \cos \theta}{H_{c2}^c} \right| = 1 \quad (1)$$

where  $H_{c2}^{ab}$  and  $H_{c2}^c$  are the upper critical fields for field applied in-plane and out-of-plane, respectively (33). The response of  $\text{Ba}_6\text{Nb}_{11}\text{S}_{28}$  can be fit by such a form, contrasting the anisotropic 3D character of  $2\text{H-NbS}_2$  (17) (fig. S25). Furthermore, for  $\text{Ba}_6\text{Nb}_{11}\text{S}_{28}$ , we observe an enhancement of the scale of  $\mu_0 H_{c2}(\theta)$  for angles below  $1.7^\circ$  measured relative to the  $ab$ -plane. As shown in the inset of Fig. 3C, this anomalous enhancement coincides with  $\mu_0 H_{c2}(\theta)$  crossing the Pauli paramagnetic limit  $\mu_0 H_P \approx 1.84 T_{\text{BKT}} = 1.51$  T. We find that two independent Tinkham fits trace the data across the entire angular regime: For  $|\theta - 90^\circ| \geq 1.7^\circ$  we have  $\mu_0 H_{c2}^c = 0.15$  T,  $\mu_0 H_{c2}^{ab} = 2.19$  T, and for  $|\theta - 90^\circ| \leq 1.7^\circ$  we obtain  $\mu_0 H_{c2}^c = 0.09$  T,  $\mu_0 H_{c2}^{ab} = 2.55$  T.

To further examine the anomaly in  $\mu_0 H_{c2}$ , we measured  $\rho_{xx}(H, T)$  with  $\theta$  systematically tuned away from  $90^\circ$ . Plotted as the excess conductivity  $\delta\sigma \equiv 1 - (\rho_{xx}/\rho_{xx}^N)$ , the substantial

enhancement at low  $T$  and high  $H$  quickly disappears as  $\theta$  is moved away from  $90^\circ$ , and by  $\theta = 86^\circ$  there is little variation with further field tilt (Fig. 4A). A distinct feature at all values of  $\theta$  is the finite  $\delta\sigma$  associated with fluctuating superconductivity for low  $H$  extending to  $T$  beyond  $T_{\text{BKT}}$ . To remove this fluctuation contribution, we plot the difference  $\delta\sigma(\theta = 90^\circ) - \delta\sigma(\theta = 84^\circ)$  in Fig. 4B. The expected 2D Ginzburg-Landau behavior is shown as a green curve; the transition curve follows this response below  $T_{\text{BKT}}$  until  $T/T_{\text{BKT}} \approx 0.6$ , below which a considerable enhancement is observed. As shown in Fig. 4C, this behavior is confined to low temperature and to a small angular region  $\delta\theta$  about the  $ab$ -plane.

These observations taken together indicate the appearance of a clean 2D superconducting state with enhanced stability (larger  $H_{c2}$ ) when  $T < 0.5 T_c$  and field  $H > H_P$  applied very close to the layer plane. Various theoretical scenarios have been discussed for Pauli breaking in 2D superconductors, including spin-orbit scattering (34), Ising superconductivity (19–21), and Fulde-Ferrell-Larkin-Ovchinnikov (FFLO) states (1, 2). Given the clean-limit superconductivity realized here, spin-orbit scattering enhancements cannot account for the present observations. The dominant local Rashba spin-orbit coupling in the present system reduces the importance of the local Ising coupling (35), and in Ising superconductors no

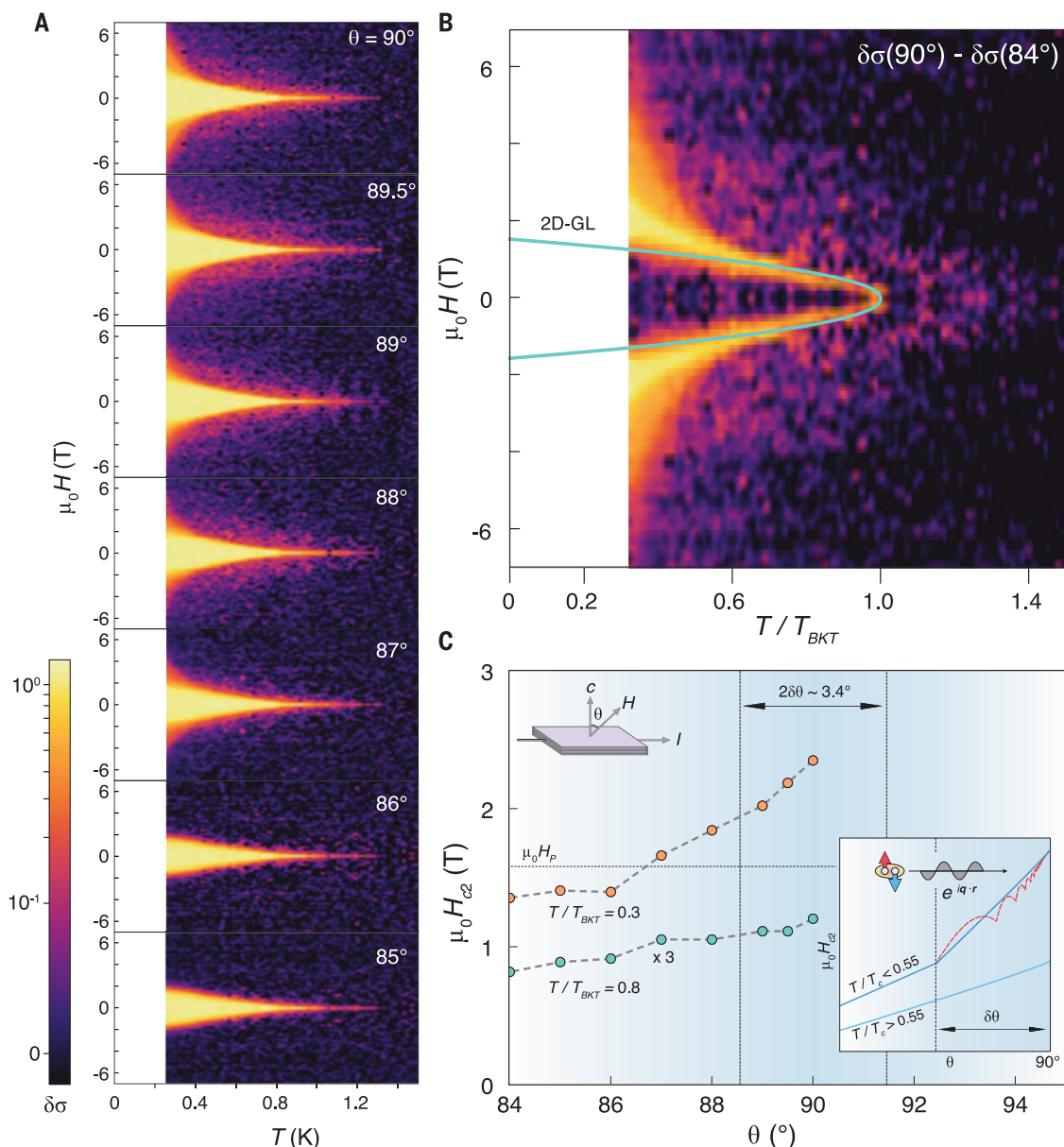


**Fig. 4. Superconducting phase diagram of  $\text{Ba}_6\text{Nb}_{11}\text{S}_{28}$ .** (A) Excess conductivity relative to the normal state  $\delta\sigma(\mu_0 H, T)$  for field angles  $\theta$  near the  $ab$ -plane ( $\theta = 90^\circ$ ). (B) Difference between  $\delta\sigma(\mu_0 H, T)$  for  $\theta = 90^\circ$  and  $\theta = 84^\circ$ . The temperature axis is normalized to  $T_{BKT}$ . The green curve represents the 2D Ginzburg-Landau (2D-GL) model of  $\mu_0 H_{c2}$ . (C) Angular dependence of  $\mu_0 H_{c2}$  at  $T/T_{BKT} = 0.3$  (orange) and  $\mu_0 H_{c2}$  at  $T/T_{BKT} = 0.8$  (green, magnified by a factor of 3). Inset: Schematic depiction

of  $\mu_0 H_{c2}$  in a clean 2D system where an enhancement is expected within a critical region  $|\theta - 90^\circ| < \delta\theta$  where orbital limiting is quenched and an FFLO state, characterized by a superconducting gap  $\Delta$  of the form  $\exp(iq \cdot r)$ , appears for  $T/T_c < 0.55$  and  $H > H_p$  (dark blue solid line). Theoretical studies of 2D FFLO superconductors further predict a cascade of magnetic vortex states that appear as a corrugation of  $\mu_0 H_{c2}(\theta)$  within this regime (37) (red dashed line).

abrupt change in  $H_{c2}(\theta)$  is expected. Instead, the sharp angle-dependent enhancement resembles that of the clean layered organic FFLO candidate  $\beta''\text{-(ET)}_2\text{SF}_5\text{CH}_2\text{CF}_2\text{SO}_3$  [where ET is bis(ethylenedithio)tetrathiafulvalene] in similar conditions of  $H$  and  $T$  arising when the orbital limiting of superconductivity is quenched by aligning  $H$  close to the layer plane (36). As shown schematically in the inset of Fig. 4C, once orbital limiting is overcome within a critical angular window  $\delta\theta$  [typically on the order of  $1^\circ$  to  $2^\circ$  in organic systems (37)], one naturally

expects a sharp enhancement of  $H_{c2}(\theta)$  as the large in-plane magnetic field stabilizes a finite-momentum pairing state.

The close parallel between our observations and those expected for a 2D FFLO phase [along with our ability to fit the phase diagram in Fig. 4B with predictions for such a phase (27)] highlights it as a promising candidate. Theoretical studies of 2D FFLO superconductors further predict a cascade of magnetic vortex states with finite momentum for  $T/T_c < 0.55$ ,  $H > H_p$ , and  $|\theta - 90^\circ| < \delta\theta$  (Fig. 4C,

inset, red dashed line), which may be resolved by higher-resolution measurements. More directly, relative to clean 2D organic superconductors (Fig. 1A), the robust inorganic nature of  $\text{Ba}_6\text{Nb}_{11}\text{S}_{28}$  offers the opportunity to examine the potential real-space modulation of superconductivity—using, for example, scattering techniques (38). Unlike other clean inorganic systems,  $\text{Ba}_6\text{Nb}_{11}\text{S}_{28}$  is derived from a well-studied family of materials, lacks localized magnetic moments, and, perhaps most important, has vdW layer bonding that allows for

exfoliation and integration into superconducting device structures. One exciting consequence could be simplified fabrication of phase-sensitive junction devices similar to those used to study the cuprates and other unconventional superconductors (39).

We hypothesize that the large enhancement of electronic mobility observed for the  $H\text{-NbS}_2$  layers in  $\text{Ba}_6\text{Nb}_{11}\text{S}_{28}$  is attributable to screening by the highly polarizable block layer akin to that observed in engineered semiconductor heterostructures (40). Additionally, our density functional theory (DFT) calculations suggest that the lowest-energy cleavage occurs between the  $H\text{-MX}_2$  and block layers, implying that mechanically exfoliated  $\text{Ba}_6\text{Nb}_{11}\text{S}_{28}$  may yield naturally encapsulated  $H\text{-NbS}_2$  monolayers akin to vdW structures made by stacking  $\text{MX}_2$  layers and h-BN (22). [We observe, using optical and atomic force microscopy, that standard exfoliation techniques can be used to obtain flakes suitable for device fabrication (17).] However, given that bulk  $\text{Ba}_6\text{Nb}_{11}\text{S}_{28}$  already exhibits two-dimensional physics, we propose that insertion of commensurate spacer layers could be an alternative to fabricating exfoliated nanodevices. There is also scope for functionalizing the spacer layer to further modulate the  $H\text{-MX}_2$  layer—for example, by introducing magnetic constituents. The large electronic mean free path of  $\text{Ba}_6\text{Nb}_{11}\text{S}_{28}$  enables clean-limit superconductivity and can potentially realize unconventional phases predicted in monolayer  $H\text{-MX}_2$  superconductors (3, 4, 41, 42). The physics of other  $\text{MX}_2$  materials can also benefit from longer electron mean free paths. In particular, extending the materials family of  $\text{MX}_2$  natural commensurate superlattices may, for example, pave the way to longer mean free paths, which would enable topological edge mode circuitry in  $\text{WTe}_2$  superlattices (43) or longer exciton lifetimes in  $\text{MoS}_2$  and related semiconducting TMD materials (44).

## REFERENCES AND NOTES

1. L. N. Bulaeviskii, *Sov. Phys. JETP* **38**, 634–639 (1973).
2. L. N. Bulaeviskii, *Sov. Phys. JETP* **37**, 1133–1136 (1973).
3. B. T. Zhou, N. F. Q. Yuan, H. L. Jiang, K. T. Law, *Phys. Rev. B* **93**, 180501 (2016).
4. C.-X. Liu, *Phys. Rev. Lett.* **118**, 087001 (2017).
5. A. F. Hebard, A. T. Fiory, *Phys. Rev. Lett.* **44**, 291–294 (1980).
6. D. B. Haviland, Y. Liu, A. M. Goldman, *Phys. Rev. Lett.* **62**, 2180–2183 (1989).
7. J. W. P. Hsu, A. Kapitulnik, *Phys. Rev. B* **45**, 4819–4835 (1992).
8. N. Reyren *et al.*, *Science* **317**, 1196–1199 (2007).
9. Y. Kozuka *et al.*, *Nature* **462**, 487–490 (2009).
10. C. Park, R. L. Snyder, *J. Am. Ceram. Soc.* **78**, 3171–3194 (1995).
11. P. A. Lee, N. Nagaosa, X.-G. Wen, *Rev. Mod. Phys.* **78**, 17–85 (2006).
12. A. P. Mackenzie, Y. Maeno, *Rev. Mod. Phys.* **75**, 657–712 (2003).
13. J. Singleton, C. Mielke, *Contemp. Phys.* **43**, 63–96 (2002).
14. M. Smidman, M. B. Salamon, H. Q. Yuan, D. F. Agterberg, *Rep. Prog. Phys.* **80**, 036501 (2017).
15. F. R. Gamble, F. J. Disalvo, R. A. Klemm, T. H. Geballe, *Science* **168**, 568–570 (1970).
16. A. Meerschaut, *Curr. Opin. Solid State Mater. Sci.* **1**, 250–259 (1996).
17. See supplementary materials.
18. D. Xiao, G. B. Liu, W. Feng, X. Xu, W. Yao, *Phys. Rev. Lett.* **108**, 196802 (2012).
19. J. M. Lu *et al.*, *Science* **350**, 1353–1357 (2015).
20. Y. Saito *et al.*, *Nat. Phys.* **12**, 144–149 (2016).
21. X. Xi *et al.*, *Nat. Phys.* **12**, 139–143 (2016).
22. S. Manzeli, D. Ovchinnikov, D. Pasquier, O. V. Yazyev, A. Kis, *Nat. Rev. Mater.* **2**, 17033 (2017).
23. Y. A. Bychkov, E. I. Rashba, *JETP Lett.* **39**, 78–81 (1984).
24. B. Morosin, *Acta Crystallogr. B* **30**, 551–552 (1974).
25. X. Zhang, Q. Liu, J. W. Luo, A. J. Freeman, A. Zunger, *Nat. Phys.* **10**, 387–393 (2014).
26. J. M. Riley *et al.*, *Nat. Phys.* **10**, 835–839 (2014).
27. M. Naito, S. Tanaka, *J. Phys. Soc. Jpn.* **51**, 219–227 (1982).
28. Y. Hamaue, R. Aoki, *J. Phys. Soc. Jpn.* **55**, 1327–1335 (1986).
29. B. I. Halperin, D. R. Nelson, *J. Low Temp. Phys.* **36**, 599–616 (1979).
30. Q. Li, M. Hückler, G. D. Gu, A. M. Tsvetlik, J. M. Tranquada, *Phys. Rev. Lett.* **99**, 067001 (2007).
31. C. Heil, M. Schlupf, F. Giustino, *Phys. Rev. B* **98**, 075120 (2018).
32. D. H. Kim, A. M. Goldman, J. H. Kang, R. T. Kampwirth, *Phys. Rev. B* **40**, 8834–8839 (1989).
33. M. Tinkham, *Introduction to Superconductivity* (Dover, ed. 2, 2004).
34. R. A. Klemm, A. Luther, M. R. Beasley, *Phys. Rev. B* **12**, 877–891 (1975).
35. J. Falson *et al.*, *Science* **367**, 1454–1457 (2020).
36. R. Beyer, B. Bergk, S. Yasin, J. A. Schlueter, J. Wosnitza, *Phys. Rev. Lett.* **109**, 027003 (2012).
37. H. Shimahara, D. Rainer, *J. Phys. Soc. Jpn.* **66**, 3591–3599 (1997).
38. A. Huxley *et al.*, *Nature* **406**, 160–164 (2000).
39. D. J. Van Harlingen, *Rev. Mod. Phys.* **67**, 515–535 (1995).
40. D. Jena, A. Konar, *Phys. Rev. Lett.* **98**, 136805 (2007).
41. Y. Nakamura, Y. Yanase, *Phys. Rev. B* **96**, 054501 (2017).
42. L. Wang, T. O. Rosdahl, D. Sticlet, *Phys. Rev. B* **98**, 205411 (2018).
43. Z. Fei *et al.*, *Nat. Phys.* **13**, 677–682 (2017).
44. G. Wang *et al.*, *Rev. Mod. Phys.* **90**, 021001 (2018).
45. A. Devarakonda, H. Inoue, S. Fang, C. Ozsoy-Keskinbora, T. Suzuki, M. Kriener, L. Fu, E. Kaxiras, D. C. Bell, J. G. Checkelsky, Data for “Clean 2D superconductivity in a bulk van der Waals superlattice”, Harvard Dataverse (2020); doi:10.7910/DVN/GSYOYA.

## ACKNOWLEDGMENTS

We thank Y. Tokura, P. A. Lee, M. Nakano, H. Matsuoka, N. F. Q. Yuan, V. Mitrovic, and S.-L. Zheng for fruitful discussions, and M. Kamitani and A. Akey for technical support. **Funding:** Supported by the Gordon and Betty Moore Foundation through grants GBMF3848 and GBMF9070 to J.G.C. (instrumentation development); the Office of Naval Research (ONR) under award N00014-17-1-2883 (advanced characterization); the U.S. Department of Energy (DOE) Office of Science, Basic Energy Sciences, under award DE-SC0019300 (material development); the STC Center for Integrated Quantum Materials, NSF grant DMR-1231319 (A.D., S.F., C.O.-K., and E.K.); and the DOE Office of Basic Energy Sciences under award DE-SC0018945 (L.F.). Computations were performed on the Odyssey cluster supported by the FAS Division of Science, Research Computing Group at Harvard University, and the Extreme Science and Engineering Discovery Environment (XSEDE), which is supported by NSF grant ACI-1548562. A portion of this work was performed at the National High Magnetic Field Laboratory, which is supported by NSF Cooperative Agreement DMR-1157490, the State of Florida, and DOE. **Author contributions:** A.D. synthesized and characterized the single crystals. A.D. and H.I. performed the electrical transport experiments; A.D. and M.K. performed the magnetization experiments; C.O.-K. and D.C.B. performed the electronic microscopy experiments; A.D. and S.F. performed theoretical calculations; all authors contributed to discussions and writing of the manuscript; and J.G.C. coordinated the project. **Competing interests:** The authors declare no competing interests. **Data and materials availability:** The data in the manuscript are available from the Harvard Dataverse (45).

## SUPPLEMENTARY MATERIALS

science.sciencemag.org/content/370/6513/231/suppl/DC1  
Materials and Methods  
Supplementary Text  
Figs. S1 to S26  
Tables S1 to S6  
References (46–154)

28 September 2019; accepted 21 August 2020  
10.1126/science.aaz6643

## Clean 2D superconductivity in a bulk van der Waals superlattice

A. Devarakonda, H. Inoue, S. Fang, C. Ozsoy-Keskinbora, T. Suzuki, M. Kriener, L. Fu, E. Kaxiras, D. C. Bell and J. G. Checkelsky

*Science* **370** (6513), 231-236.  
DOI: 10.1126/science.aaz6643

### Alternative route to a 2D superconductor

Single layers of transition metal dichalcogenides exhibit exotic properties, including superconductivity. The usual route to obtaining such samples is to exfoliate a three-dimensional (3D) crystal. Devarakonda *et al.* instead grew a superlattice comprising alternating layers of the transition metal dichalcogenide hexagonal NbS<sub>2</sub> and the material Ba<sub>3</sub>NbS<sub>5</sub> (see the Perspective by Schoop). The inert Ba<sub>3</sub>NbS<sub>5</sub> layers serve to dissociate the superconducting NbS<sub>2</sub> layers from one another, resulting in 2D superconductivity with high carrier mobility. The combination of high mobility and reduced dimensionality may give rise to exotic quantum phases.

*Science*, this issue p. 231 see also p. 170

#### ARTICLE TOOLS

<http://science.sciencemag.org/content/370/6513/231>

#### SUPPLEMENTARY MATERIALS

<http://science.sciencemag.org/content/suppl/2020/10/07/370.6513.231.DC1>

#### RELATED CONTENT

<http://science.sciencemag.org/content/sci/370/6513/170.full>

#### REFERENCES

This article cites 153 articles, 6 of which you can access for free  
<http://science.sciencemag.org/content/370/6513/231#BIBL>

#### PERMISSIONS

<http://www.sciencemag.org/help/reprints-and-permissions>

Use of this article is subject to the [Terms of Service](#)

*Science* (print ISSN 0036-8075; online ISSN 1095-9203) is published by the American Association for the Advancement of Science, 1200 New York Avenue NW, Washington, DC 20005. The title *Science* is a registered trademark of AAAS.

Copyright © 2020 The Authors, some rights reserved; exclusive licensee American Association for the Advancement of Science. No claim to original U.S. Government Works